Supplementary Information

Size-controlled liquid phase synthesis of colloidally stable Co$_3$O$_4$ nanoparticles

Johannes Kießling,*[a] Sabine Rosenfeldt,[b,c] and Anna S. Schenk*[a,c]

[a] *Physical Chemistry IV, University of Bayreuth, Universitaetsstrasse 30, 95447 Bayreuth, Germany*

[b] *Physical Chemistry I, University of Bayreuth, Universitaetsstrasse 30, 95447 Bayreuth, Germany*

[c] *Bavarian Polymer Institute (BPI), University of Bayreuth, Universitaetsstrasse 30, 95447 Bayreuth, Germany*

*E-mail: johannes.kiessling@uni-bayreuth.de

                anna.schenk@uni-bayreuth.de

Contents

1. **Experimental Details on Nanoparticle Synthesis & Purification**
2. **Supplementary Figures and Analyses**
3. **References**

1. Experimental Details on Nanoparticle Synthesis & Purification

1.1 Reaction procedures & conditions

Based on the general synthetic protocol provided in the main text, experimental details for the preparation of spherical (S3, S4, S5) and cuboidal (Cb8, Cb11, Cb13) nanoparticles (NPs) of different sizes are summarized below.

1.1.1 Small spherical particles

Co(NO$_3$)$_2$·6 H$_2$O (2 mmol, 0.582 g) was dissolved in 20 mL oleylamine (OLA) in a sealed three-necked flask with 2 mL of EtOH as a phase mediator. The reaction mixture was purged with nitrogen at low pressure (0.5 bar) for 60 min at 50°C. Subsequently, the nitrogen flow was stopped and the experimental setup was sealed. For the precipitation of green hydroxide-based precursor particles, a base (either TBAH or NaOH) was added dropwise over 15 min, and the reaction was subsequently stirred for a further 45 min at 50°C. Afterwards, the reaction was cooled down to room temperature (RT) with a water bath, and the low boiling co-solvents (EtOH, H$_2$O, or MeOH) were removed *in vacuo*. When the boiling subsided, the temperature was increased to 50°C and held for 30 min. The precursor particles were then decomposed into Co$_3$O$_4$ at 180°C under N$_2$-flow, and the reaction was allowed to proceed for 1h. The resulting nanoparticle dispersion was cooled down to RT with an ice bath, and 2 mL of oleic acid (OA) was added before stirring the solution overnight. Subsequently, the nanoparticles were precipitated with EtOH and separated by centrifugation (7500 rpm, 10 min, Allegra 64R benchtop centrifuge, Beckman Coulter), re-dispersed in heptane, and further stabilized with ca. 0.5 mL OA for at least four hours. Afterwards, the particles were purified by several centrifugation (7500 rpm, 10 min) and re-dispersion steps with EtOH and heptane to remove traces of OLA and salts. After drying, the particles were re-dispersed in heptane and filtered through a 0.2 µm polytetrafluoroethylene (PTFE) syringe filter. **Table S1** summarizes specific experimental parameters and modifications leading to spherical NPs with ~3 nm, ~4 nm, or ~5 nm diameter. Corresponding count-size histograms are shown in **Figure S3**.

The particles depicted in **Figures 2a** and **b** were synthesized at temperatures of 50°C and 60°C in air. Otherwise, the reaction protocol described above was not altered.

Table S1: Specific experimental parameters and modifications to the general reaction procedure yielding spherical Co_3O_4 NPs with dedicated sizes.

Sample	Size [nm]	Specific procedures & parameters
S3	3	4 mL tetrabutylammonium hydroxide solution (TBAH/1.0 M in MeOH, 4 mmol) added dropwise over 15 min, no EtOH (as phase mediator) in reaction Final precipitation step: +200 vol% EtOH
S4	4	NaOH solution (2.0 M in H_2O, 4 mmol) added dropwise over 15 min Final precipitation step: +150 vol% EtOH
S5	5	NaOH solution (2.0 M in H_2O, 4 mmol) added by instant injection followed by 60 min stirring at 50°C Final precipitation step: +150 vol% EtOH

1.1.2 Cuboid particles

$Co(NO_3)_2 \cdot 6\,H_2O$ (2 mmol, 0.582 g) was dissolved in 20 mL OLA in a sealed three-necked flask with 2 mL of EtOH as phase mediator, and the mixture was subsequently stirred at 80°C for 30 min. For the precipitation of hydroxide-based precursor particles with a green-brown to brown colour, 2 mL NaOH solution (2.0 M in H_2O, 4 mmol) was injected, followed by stirring at 80°C for 1h. Afterwards, the reaction was cooled down to RT with a water bath, and the low boiling co-solvents (H_2O and EtOH) were removed *in vacuo*. When the boiling subsided, the temperature was increased to 80°C and held for 30 min. The precursor particles were then decomposed into Co_3O_4 at 180°C under N_2-flow for 1 h. The resulting nanoparticle dispersion was cooled down to RT with an ice bath, and 2 mL OA was added before stirring the solution overnight. Subsequently, the nanoparticles were precipitated with +150 vol% EtOH and separated by centrifugation (7500 rpm, 10 min, Allegra 64R benchtop centrifuge, Beckman Coulter), re-dispersed in heptane, and further stabilized with ca. 0.5 mL OA for at least four hours. Afterwards, the particles were purified by several centrifugation and re-dispersion steps with EtOH and heptane to remove traces of OLA and salts. After drying, the particles were re-dispersed in heptane and filtered through a 0.2 µm PTFE syringe filter. **Table S2** summarizes specific experimental parameters and modifications leading to cuboid NPs with ~8 nm, ~11 nm, or ~13 nm diameter. Corresponding count-size histograms are shown in **Figure S3**.

The particles depicted in **Figures 2c** and **e** were synthesized at 70°C and 90°C in air. Otherwise, the reaction protocol described above was not altered.

Table S2: Specific experimental parameters and modifications to the general reaction procedure yielding cuboid Co_3O_4 NPs with dedicated sizes.

Sample	Size [nm]	Specific procedures & parameters
Cb8	8	After stirring the reaction for 30 min at 80°C, the temperature is further increased to 100°C and the system is equilibrated for 5 min before the injection of NaOH. The temperature is held at 100°C for 1 h. Final precipitation step: +100 vol% EtOH
Cb11	11	The stirring time of the solution at 80°C is reduced to 10 min before the injection of NaOH. The temperature is held at 80°C for 1 h. Final precipitation step: +100 vol% EtOH Final work-up: +100 vol% EtOH
Cb13	13	No further modifications to the general procedure Final precipitation step: +75 vol% EtOH

1.2 Purification by size-selective precipitation

The particle size distribution can be narrowed further by post-synthetic removal of large (> 15-20 nm) or very small (2-5 nm) NPs by-products as demonstrated in **Figure S8** for a representative sample of Cb13 particles. For that purpose, EtOH was used as an anti-solvent. In the following procedures, the amounts of the precipitation agent are expressed as additions relative to the volume of the NP dispersion (+x vol%). The latter commonly comprised 10 mL of heptane in the here presented experiments.

Specifically, particles > 15-20 nm were removed by adding +10-30 vol% (*i.e.* corresponding to an absolute volume of 1-3 mL) of EtOH to the NP dispersion followed by centrifugation. The larger the intended particle size, the less anti-solvent should be used to prevent product loss.

Very small particles (2-5 nm) were separated with the supernatant by adding a smaller volume of EtOH for the final centrifugation step than used in **Table S1**. In these experiments, very small NPs remain in the supernatant and may be conveniently decanted. In samples S3-S5, where very small particles are the intended product, any larger impurities may be removed accordingly. After decanting, the supernatant is precipitated with up to +200 vol% EtOH (**Table S1**).

All purification steps should be performed after sufficiently stabilizing the particles with OA to prevent agglomeration during the precipitation/centrifugation cycles.

2. Supplementary Figures and Analyses

2.1 Progression of the reaction

(i) Reaction steps.

The photographs depicted in **Figure S1** display the progression of a typical NP reaction at 80°C. Due to the concentration of the reagents ($[Co^{2+}]$ = 0.1 M), the red salt solution (I) appears almost black (a red tint may be observed around the magnetic stirrer). Upon the injection of the base (II), the solution turns dark green, indicative of the formation of α-Co(OH)$_2$. After an hour of stirring (here at 80°C), a color change to greenish-brown is observed (III). Under air, the dispersion turns brown over time. After precursor decomposition at 180°C, a brown-black Co$_3$O$_4$ NP dispersion (IV) is received.
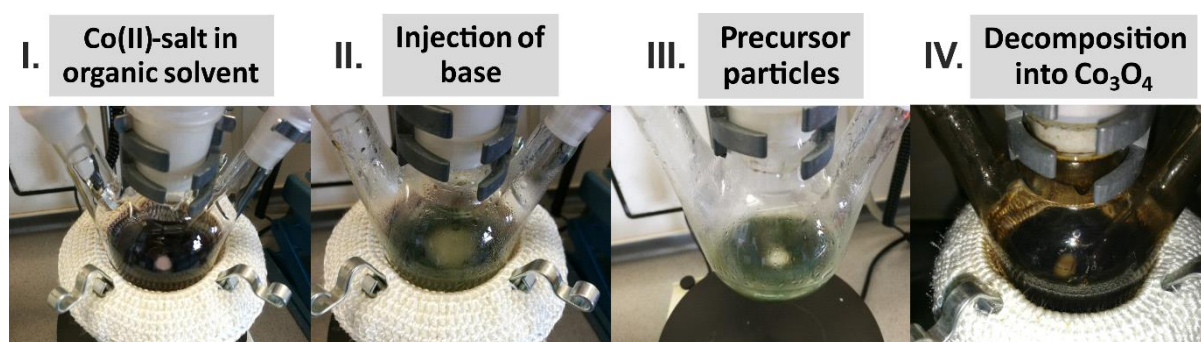

| I. Co(II)-salt in organic solvent | II. Injection of base | III. Precursor particles | IV. Decomposition into Co$_3$O$_4$ |

Figure S1: Progression of a typical NP synthesis at 80°C in a three-necked round-bottomed flask. From left to right: (I) Co(NO$_3$)$_2$ in oleylamine. (II) Hydroxide precursor formation after injection of base (here: NaOH). (III) Nucleation and growth of precursor particles. (IV) Co$_3$O$_4$ NPs in suspension after thermal decomposition of the precursor.

(ii) X-ray diffraction analysis of intermediates and ex-situ thermal conversion products

In order to obtain further insights into the pathway of the reaction, batches of samples S5 (50°C, green powder) and Cb13 (80°C, dark brown powder) were quenched after the formation of precursor particles (*i.e.* before thermal conversion to Co$_3$O$_4$) and prepared as dry powders for XRD measurements as displayed in **Figure S2**. For reference, an additional brucite-type β-Co(OH)$_2$ was synthesized at room temperature by substituting OLA with water under a N$_2$ atmosphere (pink curve) and the diffractogram of the phase-pure, pink precipitate may be assigned to literature-reported data of β-Co(OH).[1]

Sample S5 (green curve) matches well with published diffractograms of α-Co(OH)$_2$ and cobalt-containing hydrotalcite structures.[1–4] Two weak reflexes at ca. 45° and 55° attributed to α-Co(OH)$_2$ are missing in the diffractogram of S5 though, which may be explained by either a poor signal-to-noise ratio or systematic extinction caused by intercalation of water or foreign ions into the layered crystallographic structure. A comparison to the diffractogram of the pink brucite Co(OH)$_2$ power proves that β-Co(OH)$_2$ is also present as a minority phase in S5, which is in agreement with a report by Xu *et al.*, demonstrating that α-Co(OH)$_2$ undergoes a slow temperature-dependent conversion to β-Co(OH)$_2$ in the presence of N$_2$.[1]

The green α-Co(OH)$_2$ sample (S5) was then heat-treated *ex-situ* in the solid state at temperatures of 120°C (light brown curve), 180°C (grey curve) and 300°C (black curve), respectively for 4 h, which led to a gradual transformation of the precursor into Co$_3$O$_4$ (black curve). Please note that the phase transition takes a significantly longer amount of time in the solid state as compared to the dispersed state (*cf.* liquid phase synthesis as described in main text Chapter 1). After tempering at 120°C, the peaks of α- and β-Co(OH)$_2$ (green asterisks and pink drop lines) are still clearly present in the diffractogram, albeit with reduced intensities. The signature of β-Co(OH)$_2$ vanishes completely after heating at 180°C. Traces of the stronger α-Co(OH)$_2$ reflexes remain visible after the heat treatment, but begin to shift positions, while weak reflexes assigned to Co$_3$O$_4$ start to appear. Calcination at 300°C yields phase-pure Co$_3$O$_4$ (black drop lines).[5]

In contrast to the precursor phase of the spherical S5 NPs, the larger, cuboidal Cb13 precursor particles (dark brown curve, precipitated at 80°C) appear to occur as a complex multiphase transition state between α-Co(OH)$_2$ and Co$_3$O$_4$. Many of the Bragg reflexes can be attributed to the oxidized species CoO(OH) (brown asterisks).[6,7] The exact phase identification is complicated by the fact that CoO(OH) shares numerous reflexes with α-Co(OH)$_2$ and Co$_3$O$_4$. An unaffiliated peak at ca. 31°, however, proves that Co$_3$O$_4$ is already being formed at 80°C while simultaneously several reflexes of α-Co(OH)$_2$ are still clearly identified. One additional reflex between 31-32° seems to be related to β-Co(OH)$_2$ as seen by comparison with the diffractogram of sample S5 (precipitated at 50°C). In summary, the diffractogram provides a signature of the oxidation of an α-Co(OH)$_2$ phase to CoO(OH) in the presence of oxygen.
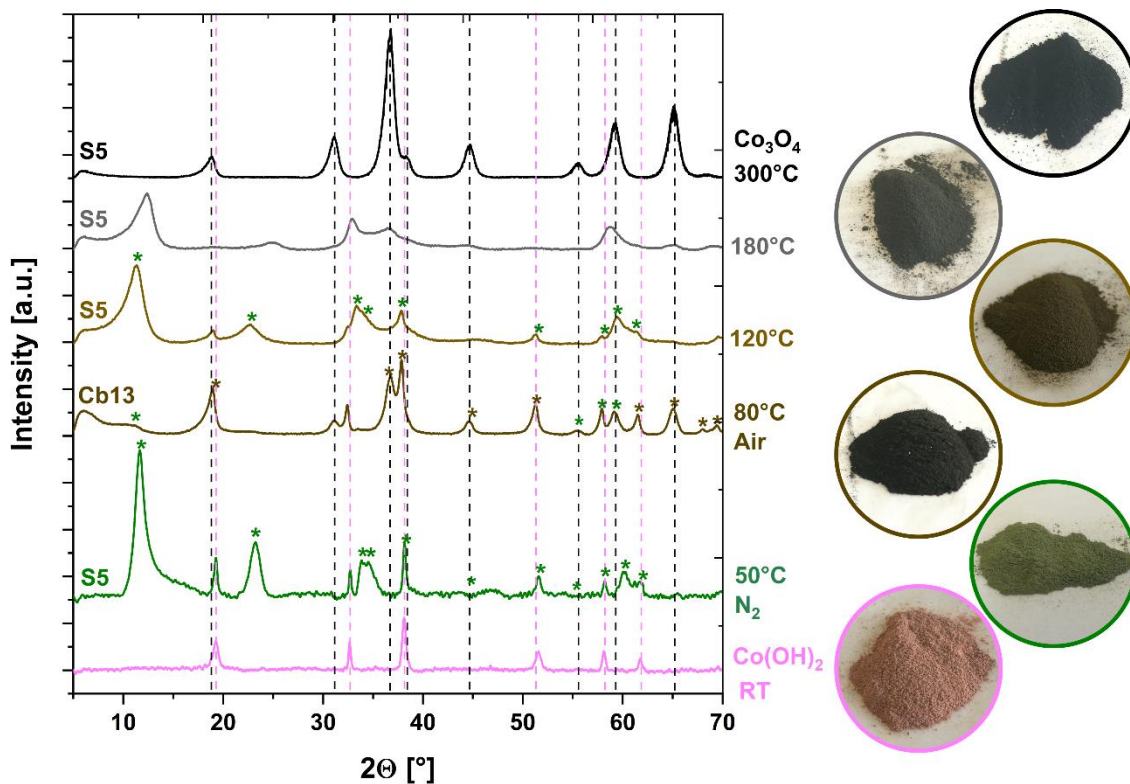
Figure S2: X-ray diffractograms obtained from powdered NPs and intermediates.

Sample S5 (green, precipitated at 50°C in N_2 atmosphere) mainly consists of α-Co(OH)$_2$, but also contains β-Co(OH)$_2$ as a minority components as can be seen by comparison with the diffraction pattern of a a control sample (pink, precipitated at room temperature). The α-Co(OH)$_2$ powder (green) was further heated at 120°C (light brown), 180°C (grey), and 300°C (black) for 4 h to induce a gradual transformation into Co$_3$O$_4$ (black). The larger cuboidal sample (Cb13, dark brown, precipitated at 80°C in air) consists of a more complex multiphase. Green asterisks indicate characteristic Bragg reflexes attributable to α-Co(OH)$_2$. Brown asterisks indicate Bragg reflexes attributed to brown CoO(OH). Pink and black droplines mark the positions of diffraction peaks assigned to β-Co(OH)$_2$ and Co$_3$O$_4$, respectively. To the right of the driffactograms photographs of the corresponding powders are shown.

2.2 Individual count-size histograms of the obtained nanoparticles

Count-size histograms were obtained from TEM image analysis of small spherical and larger cuboid (**Figure S3**) particles. The particle size distributions generally show a comparably narrow tailing profile and can be fitted by the log-normal function. While spherical NPs were obtained with average diameters between 2.8 nm and 4.8 nm (samples S3, S4, and S5), the particles with cuboid morphologies were larger with size distributions centered at 7.2 nm, 10.9 nm, and 13.2 nm (samples Cb8, Cb11, and Cb13).
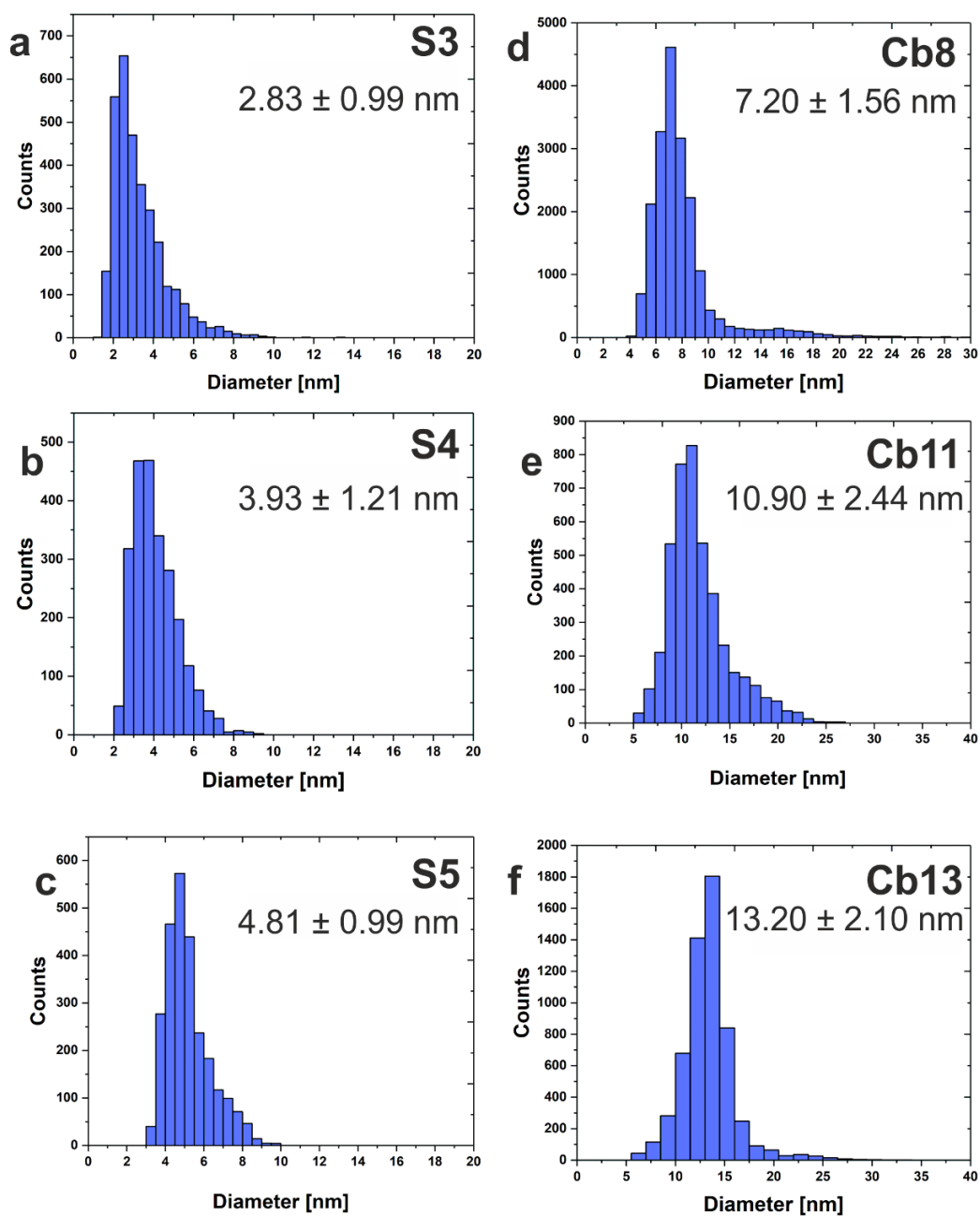
Figure S3: Count-size histograms and average particle sizes of spherical (S3, S4, S5) and cuboid (Cb8, Cb11, Cb13) nanoparticles. The particles were prepared according to the procedures detailed in sections 1.1.1 and 1.1.2, and particle size distributions were determined based on the full width at half maximum after fitting a log-normal distribution to the histograms.

2.3 Pseudomorphic transformation of Co(OH)$_2$ nanocubes to Co$_3$O$_4$

Aliquots were drawn from the reagent solution before conversion into Co$_3$O$_4$ to demonstrate that the hydroxide-based precursor particles preserve their morphology during thermal conversion as illustrated in **Figure S4**. The selected area electron diffraction (SAED) pattern of the precursor particles (**Figure S4a**) reveals that a phase mixture of Co(OH)$_2$ (green trace, COD: 1010267) and CoO(OH) (brown trace, COD: 9009884) is initially formed during the reaction (reflex indexing performed based on .cif-files). The α-Co(OH)$_2$ phase is formed by the oxidation of few Co^{2+} ions to Co^{3+}, thus increasing the interlayer distance between the stacked metal hydroxide layers and enabling the intercalation of anions and water molecules into the structure.[8] Exposure to oxygen may further oxidize the α-Co(OH)$_2$ to CoO(OH).[1] SAED phase analysis shows that both Co^{2+}- and Co^{3+}-ions are present in the precursor before thermal conversion, thus aiding the formation of the mixed-valence product Co$_3$O$_4$. Upon decomposition of the precursor at 180°C, the characteristic pattern of the spinel crystal structure emerges in SAED analysis as displayed in **Figure S4b** (white trace, COD: 9005898).

The transmission electron micrographs displayed in **Figures S4c** and **d** compare NPs obtained from an aliquot of the precursor particles before the decomposition (**Figure S4c**) at 80°C with purified particles isolated after thermal transformation at 180°C (**Figure S4d**). In both cases, the general morphology of the particles is cuboidal, even though faceting is more clearly pronounced in the mature product. Corresponding count-size histograms (**Figures S4e** and **f**) demonstrate that the average particle size does not change during the decomposition reaction.
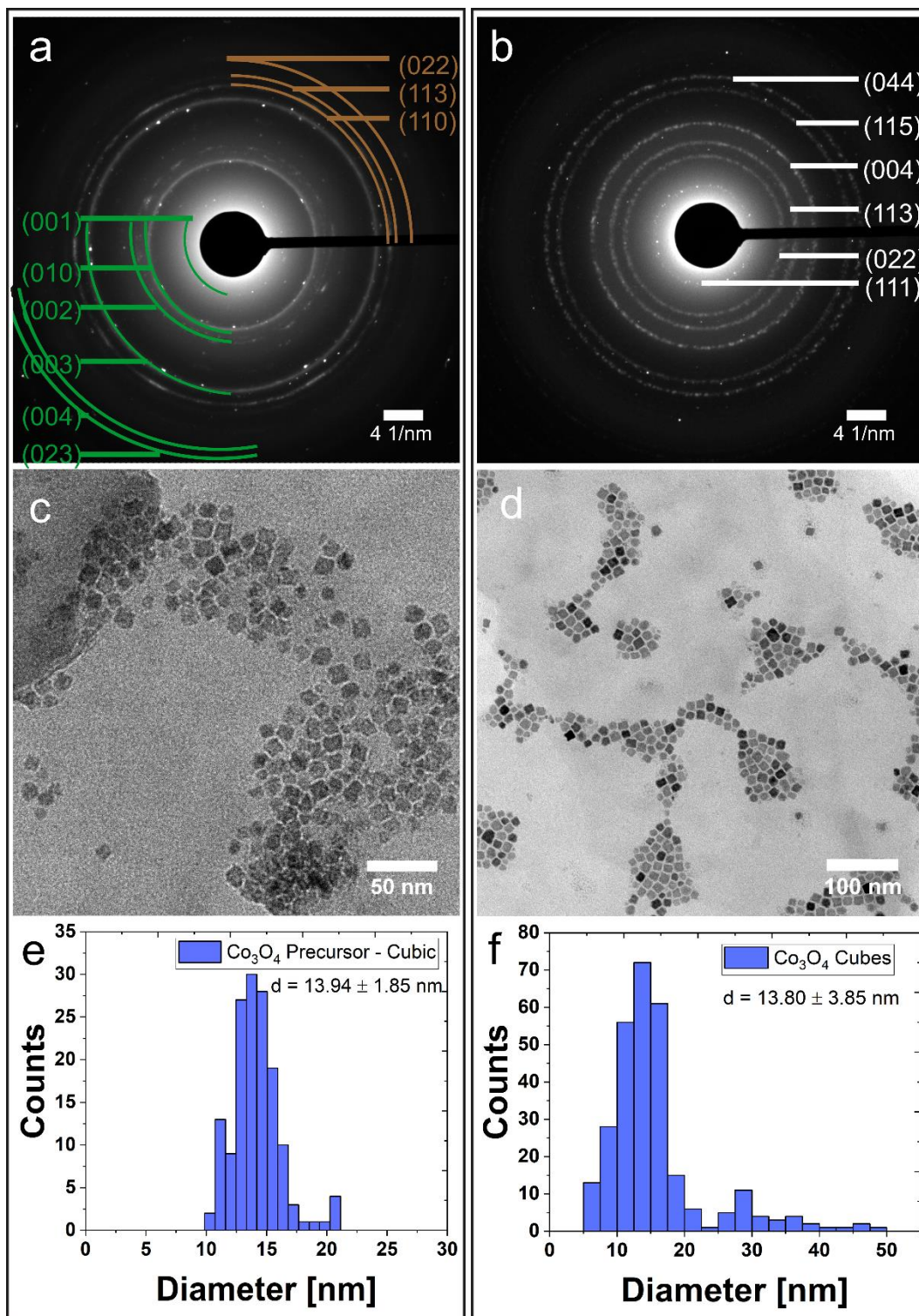
Figure S4: The thermally driven pseudomorphic transformation of the Co(OH)$_2$-based precursor into Co$_3$O$_4$ NPs. Particles were prepared according to the reaction conditions described for sample Cb13. a) SAED pattern of the hydroxide-based precursor particles. Signals attributable to lattice planes of Co(OH)$_2$ are highlighted in green, while brown circular lines mark reflections assigned to CoO(OH). b) SAED pattern of Co$_3$O$_4$ NPs with an assignment of the signals to the spinel-type cobalt(II, III) oxide structure. c) TEM micrograph obtained from an aliquot of Co(OH)$_2$ precursor particles at 80°C. d) TEM micrograph of cuboid Co$_3$O$_4$ NPs after thermal conversion. e), f) Count-size histograms corresponding to c) and d) reflecting the particle size distribution before and after thermal conversion. The particle sizes are included as insets.

2.4 Colloidal stability of Co$_3$O$_4$ nanoparticles probed by dynamic light scattering

The colloidal stability of the synthesized NPs, *i.e.* their stability against aggregation and sedimentation, was qualitatively evaluated for a dispersion of the largest obtained particles (Cb13, *cf.* **Figure 3f**) by means of dynamic light scattering (DLS; see **Figure S5**).[9] A sample of 0.03 mg/mL NPs in heptane was analyzed 10 months after the synthesis and again after 51 months of storage. After 10 months of storage at room temperature, the particles were still stable in dispersion and showed a uni-modal size distribution with a hydrodynamic radius of 15.19 ± 1.67 nm. More than four years after the synthesis, there was still no noticeable sedimentation seen by visual inspection. DLS experiments on such a long-term specimen revealed the presence of larger aggregates while the sample could not be passed through a 200 nm syringe PTFE filter. However, as a facile procedure for re-dispersion, exposure of the sample to ultrasound (US) for 10 min effectively separated NPs and aggregates into distinct fractions as displayed in **Figure S5** (red trace). After filtration through a 200 nm syringe PTFE filter, monodispersed NPs were again received (blue trace). The aggregates appeared transparent and colourless (in the syringe filter) and are presumably formed by polymerized excess oleic acid.[10] The measured hydrodynamic radius of the NPs stored for more than 4 years increased slightly to 17.57 ± 1.52 nm in this process. From these, we conclude that the NPs possess excellent inherent stability while the limiting factor is the reactivity of oleic acid.
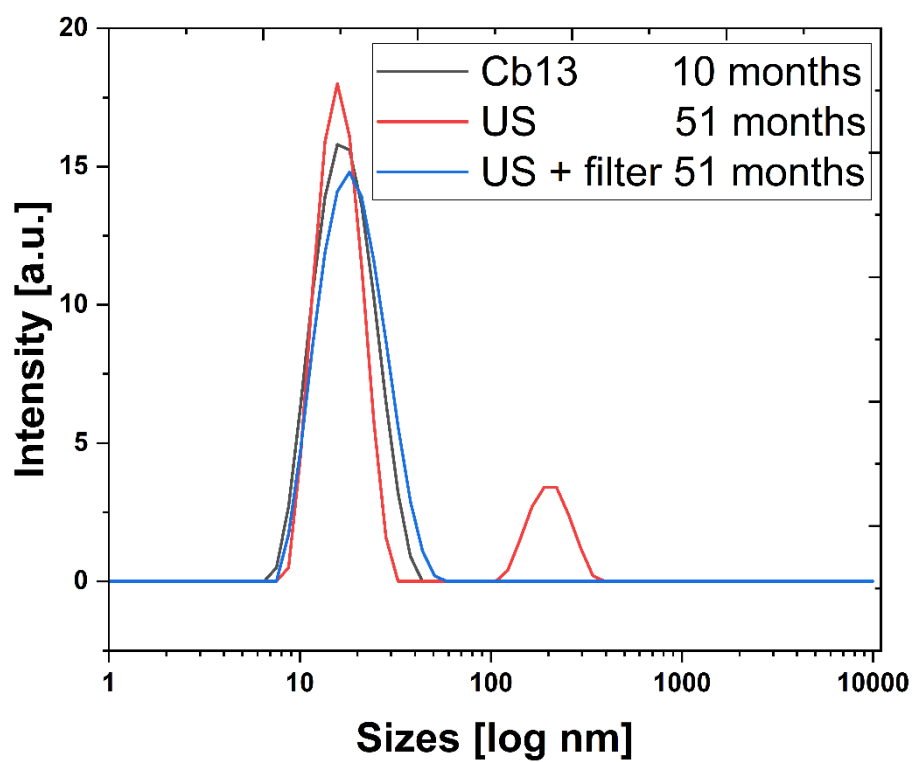
Figure S5: Dynamic light scattering frequency count-size diagram of sample Cb13. The data were acquired 10 months (black trace) and 51 months after the synthesis (red and blue traces). The latter specimen was ultrasonicated (US; red trace) and subsequently filtered (blue trace).

2.5 Precipitation with an excess of NaOH

Three equivalents of NaOH (6 mmol, 3.0 M in water) were injected into a $Co(NO_3)_2 \cdot 6 H_2O$ (2 mmol in 20 mL OLA, 2 mL EtOH) solution at 80°C, to test the effects of an excess of the base. The NPs formed under these conditions (**Figure S6**) show a smaller average size (d = 8.1 ± 4.4 nm) compared to sample Cb13 (reference system for stoichiometric addition of NaOH). Concomitantly, the particle size distribution (PSD) broadens to above 50% (PSD = 4.4 nm). Thus, a significant increase in the NaOH concentration beyond the stoichiometric amount exerts a detrimental effect on the growth reaction.
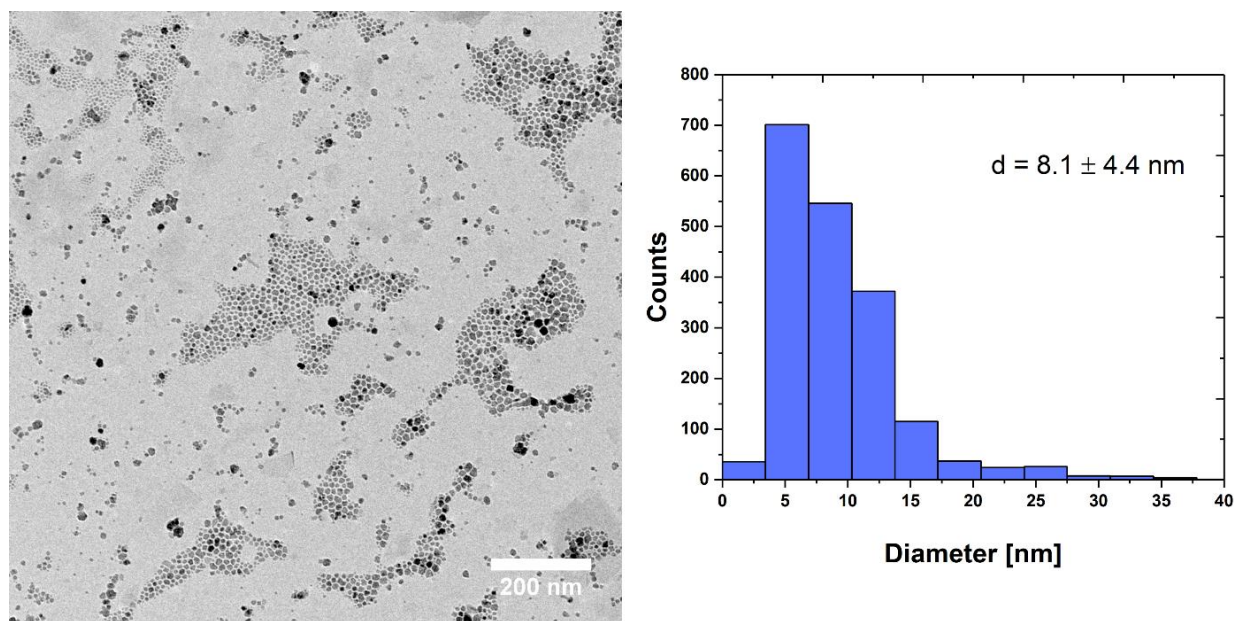
Figure S6: TEM micrograph (left) and corresponding count-size histogram (right) of synthesized particles with NaOH excess (otherwise reaction conditions according to Cb13). A significant decrease in average size accompanied by a broadening of the size distribution is observed in comparison to Cb13 (d = 13.2 ± 2.1 nm).

2.6 Complementary results on the synthesis of sample S3 in air atmosphere

Particles of the smallest size (sample S3) can be synthesized under air or nitrogen atmosphere with very similar results. A TEM micrograph and the corresponding count-size histograms of a representative batch of NPs produced under air are displayed in **Figure S7**. The NPs exhibit an average size of 3.1 ± 0.76 nm which is in very good agreement with the particle size obtained in a comparable synthesis under N_2 atmosphere (2.8 ± 1.0 nm; see **Figure 3a**). For consistency and direct comparability with samples S4 and S5 (where N_2 purging is a necessity for size control), a sample of S3 NPs prepared under N_2 atmosphere is included in **Figure 3** in the main text.
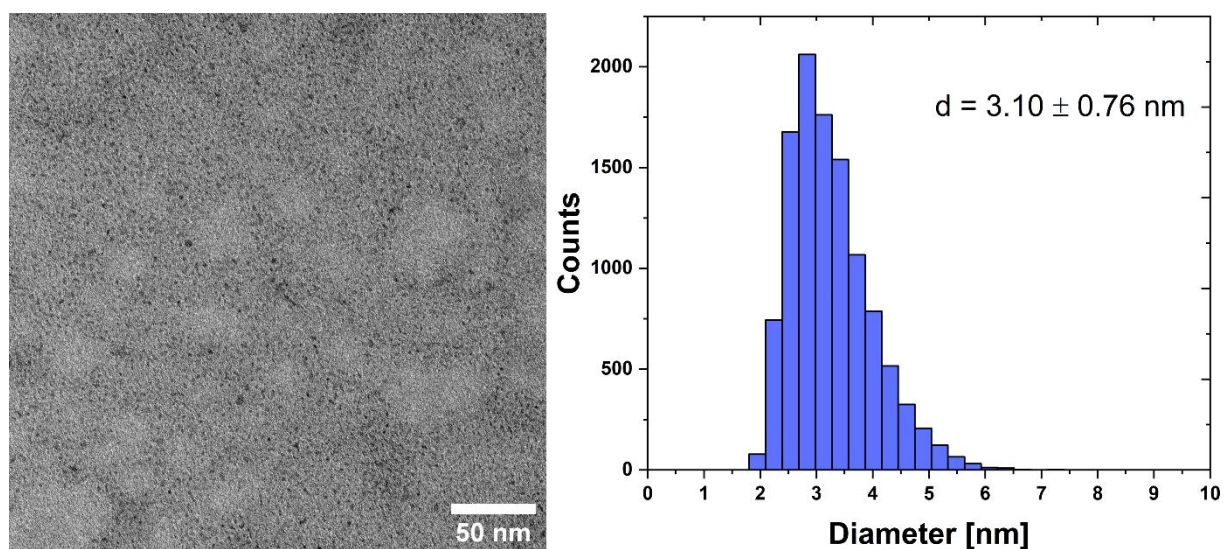

Figure S7: TEM micrograph (left) and corresponding count-size histogram (right) of sample S3 synthesized in an air atmosphere (without nitrogen purging). The resulting particles possess an average diameter of 3.1 ± 0.76 nm**.**

2.7 Size-selective precipitation procedure

Particle dimensions characteristically focus on a single size (unimodal distribution) while the distribution profiles (as seen in count-size histograms) exhibit a broad base (*cf.* **Figure 3**), it appears beneficial to include size-selective precipitation steps into the purification process to achieve artificially narrowed size distributions of the products.[11,12] By post-synthetic addition of an anti-solvent, the solubility of particles in a particular size range may be reduced, thus allowing for fractionation by centrifugation. The results of an exemplary size-selective precipitation experiment are presented in **Figure S8**.
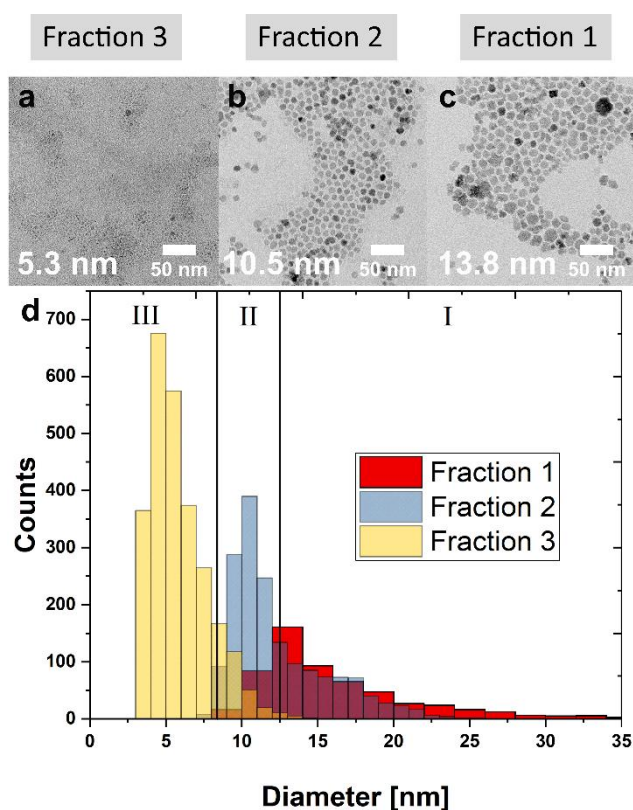

Figure S8: TEM micrographs (a-c) and corresponding count-size histograms (d) of fractions 1 to 3 produced by two size-selective precipitation steps applied to sample Cb13. Average particle sizes of a) 13.8 ± 3.2 nm (fraction 3; after size-selective precipitation with +100 vol% EtOH), b) 10.5 ± 1.5 nm (fraction 2; narrowed size distribution), and c) 5.3 ± 1.9 nm (fraction 1; after size-selective precipitation with +30 vol% EtOH) are observed, respectively.

Nanoparticles of a typical Cb13 experiment were chosen to illustrate the concept, as differences in particle size are readily apparent for these larger particles. Two consecutive precipitation steps were performed. By adding +30 vol% EtOH as an anti-solvent, the comparably few larger particles are separated in fraction 1. Equally, particularly small particles accumulate in fraction 3 after the addition of +100 vol% EtOH to the NP suspension. Consequently, the size distribution in fraction 2, where the primary mass of particles is concentrated, becomes substantially narrower.

2.8 Thermogravimetric analysis

Thermogravimetric analysis (TGA) profiles of dried oleic acid stabilized Co_3O_4 NPs are compared to pure Co_3O_4 nanopowder purchased from Sigma Aldrich and displayed in **Figure S9**. The results are displayed as relative mass change at increasing temperatures.

The Co_3O_4 control profile exhibits no mass loss until the decomposition point above 900°C which is shared by all samples. Above 900°C, Co_3O_4 undergoes a transition to CoO accompanied by a loss of oxygen.[13] The extent of the oxygen mass loss is larger with a higher initial amount of Co_3O_4 and decreases with decreasing particle size. Samples Cb8 and Cb11 with larger particles exhibit a relative mass loss of ca. 35% and 25%, respectively. Samples S3, S4, and S5 are reduced in mass by 65-70%, indicating a significantly higher amount of OA as compared to Cb8 and Cb11. Despite the high overlap of the particle size distributions of S3, S4, and S5, slight differences in the amount of OA may still be observed according to the particle size. TGA thus reveals that the relative amount of surface-bound OA is dependent on the particle size. Repeated TGA measurements reveal that the mass loss further depends on the amounts of OA used during the stabilization steps and varies if different amounts are used. The onset of mass loss begins slightly below 100°C for S3, S4, and S5, indicating remnant solvents which remain adsorbed due to the high amount of OA. For Cb8 and Cb11 the onset begins at ca. 150°C and terminates at ca. 500°C for S3. The termination point is shifting to higher temperatures for a higher amount of OA. The difference in the samples may be directly observed by the eye. Very small particles yield a grease-like substance after drying while larger particles form a brittle solid.
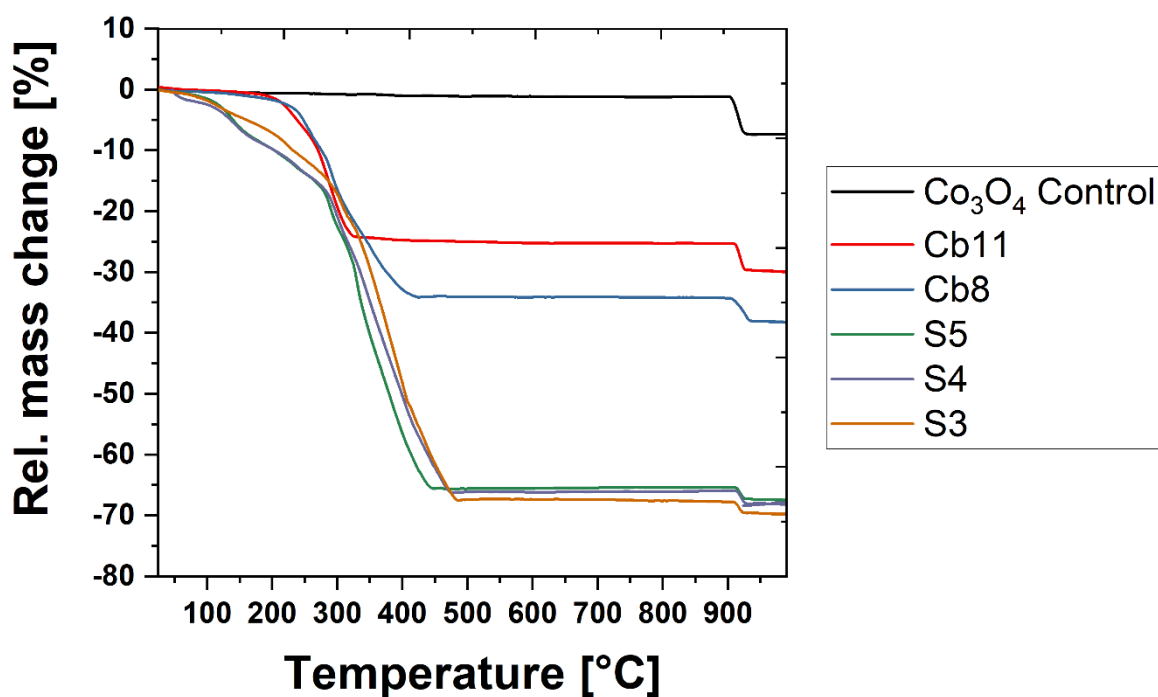

Figure S9: TGA profiles of samples S3, S4, S5, Cb8, and Cb11.The dried Co_3O_4 samples are compared to commercial Co_3O_4 nanopowder (Co_3O_4 Control) purchased from Sigma Aldrich.

2.9 Small-angle X-ray scattering of NP dispersions

Small-angle X-ray scattering (SAXS) was applied as a volume-averaging technique to quantitatively analyze the size and size distribution of the synthesized nanoparticles in complementation of semi-quantitative TEM analysis. Radially integrated scattering profiles obtained from nanoparticles in dispersion are displayed in **Figure S10** (open symbols) for samples comprising spherical (**Figure S10a**) and cuboid (**Figure S10b**) particles. Calculated scattering intensities based on the form factors of polydisperse, non-interacting homogeneous spheres are given. Very good agreement is obtained for the small particles, whereas bigger ones show deviations at small q indicating the onset of interparticle interactions, particularly in the non-diluted dispersion of the largest cuboidal particles (Cb13). The effects of interparticle interaction are further discussed in section 2.8. Nevertheless, the form factor minima are well described showing the good size selection obtained by the used synthetic protocols.
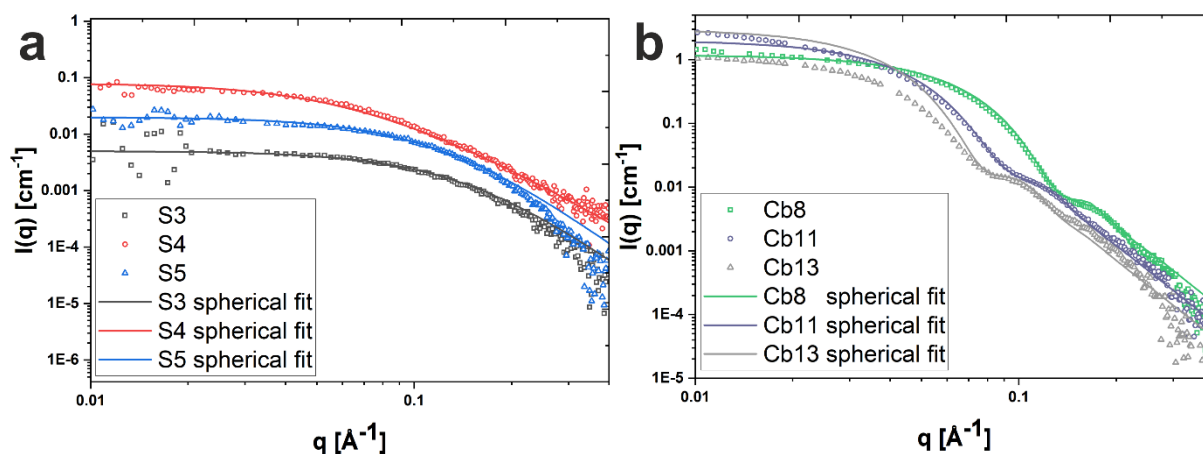

Figure S10: Radially averaged 1-dimensional SAXS intensities (open symbols) and corresponding fits based on the form factor of non-interacting homogeneous spheres for NP dispersions of samples S3-S5 (a) and Cb8-Cb13 (b). In dispersion (bulk system), the spatial orientation of cubes is averaged over all possible orientations and consequently, the contribution of the edges to the scattering signal smears out. For this reason, a cube (especially if small and polydisperse) will appear similar to a sphere of the same volume. Thus, also the sizes of nanocubes/cuboids are fitted with the model of polydisperse spheres. The fits reveal primarily isometric individual particles with diameters in the range from 2 nm to 11 nm.

2.10 Small-angle X-ray scattering of self-assembled Co$_3$O$_4$ nanoparticles

To demonstrate the influence of interparticle interactions on the scattering signal, a fresh sample of cuboidal Co$_3$O$_4$ NPs (Cb13) was dried on Kapton foil. The scattering pattern of the drop-casted Co$_3$O$_4$ NPs immobilized on Kapton is compared to the SAXS pattern of dispersed particles in hexane (**Figure S11**). The intensity at low values of q is significantly lower for the dried NPs as compared to the dispersion. The 2D pattern of the self-assembled NPs shows a pronounced Debye-Scherrer ring, reflecting interparticle interaction. The ring corresponds to a real space NP-NP distance of about 12 nm (which is similar to the edge size of a cube). The mean Feret size of Cb13 was determined by TEM as 13.65 ± 3.01 nm. If a cube of this average size is projected into a 2D plane, the latter roughly corresponds to an edge length of 9.65 nm. The discrepancy between 9.65 nm to 12 nm is presumably caused by the oleic acid ligand shell between the particles which is not visible in TEM.

The prominent Debye-Scherrer ring already demonstrates a well-defined NP-NP spacing obtained from this simple drop-casting experiment. Thus, we propose a strong potential for obtaining ordered self-assembled structures when using the herein-introduced size-dependent synthesis strategies in combination with dedicated techniques for ordered particle assembly.
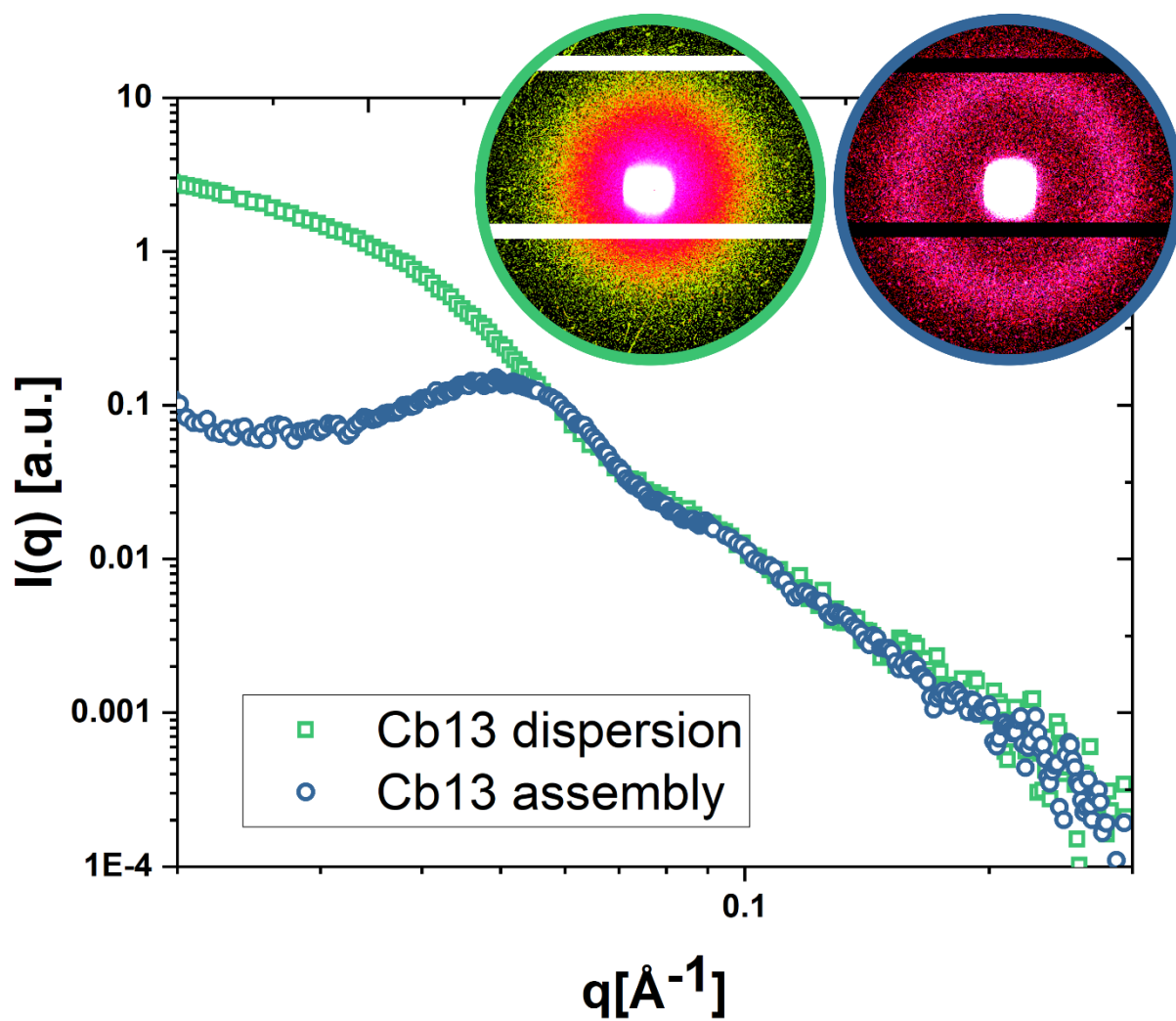
Figure S11: Comparison between cuboidal Co$_3$O$_4$ NPs (Cb13) in dispersion (green trace) and dried on Kapton foil (dark blue trace). The insets show the corresponding 2D scattering images detected for both samples. For the 1D datasets, the respective background (hexane or Kapton foil) was subtracted for better comparison.

2.11 Absorbance of Co_3O_4 NPs in the near-infrared region

Complementing the overview UV-vis and NIR spectra presented in **Figure 4**, enlarged views of relevant spectral regions in the NIR range are shown in **Figure S12** for band assignment. In agreement with literature data, significant NIR signals attributable to heptane are observed at wavelengths of 1200 nm, 1400 nm, and 1700 nm. Additionally, the third overtones of CH_2 and CH_3 stretching vibrations appear between 800-1000 nm (**Figure S12a**). The intensity distribution in the spectral range between 1100 nm and 1300 nm closely resembles the profile expected for the second overtones associated with the methyl and methylene vibrations (**Figure S12b**).[14] Between 1300 nm and 1400 nm, different modes of C-H vibrations are identified (**Figure S12c**). Buback *et al.* present a detailed analysis of the characteristic n-heptane absorption bands in the spectral range from 1650 nm to 1850 nm (**Figure S12d**), attributed to the first overtones of the CH_2 and CH_3 stretching vibrations as well as the first overtone of the cis-double bond.[15] The weaker peak at 1445 nm in **Figure S12c** represents the first overtone of the OH vibrational mode of oleic acid. It contains information on the bonding states of the ligand and is superimposed onto methyl and methylene modes which also occur in heptane.[16–18] In the liquid state, the acid groups form dimers, which significantly decrease the absorbance due to the symmetric nature of the adduct. Upon dissociation, the absorbance increases and points to the bonding of monomeric OA to the surface of the Co_3O_4 NPs. The position of the methyl and methylene bands of oleic acid coincide with those of heptane and may vary in intensity.
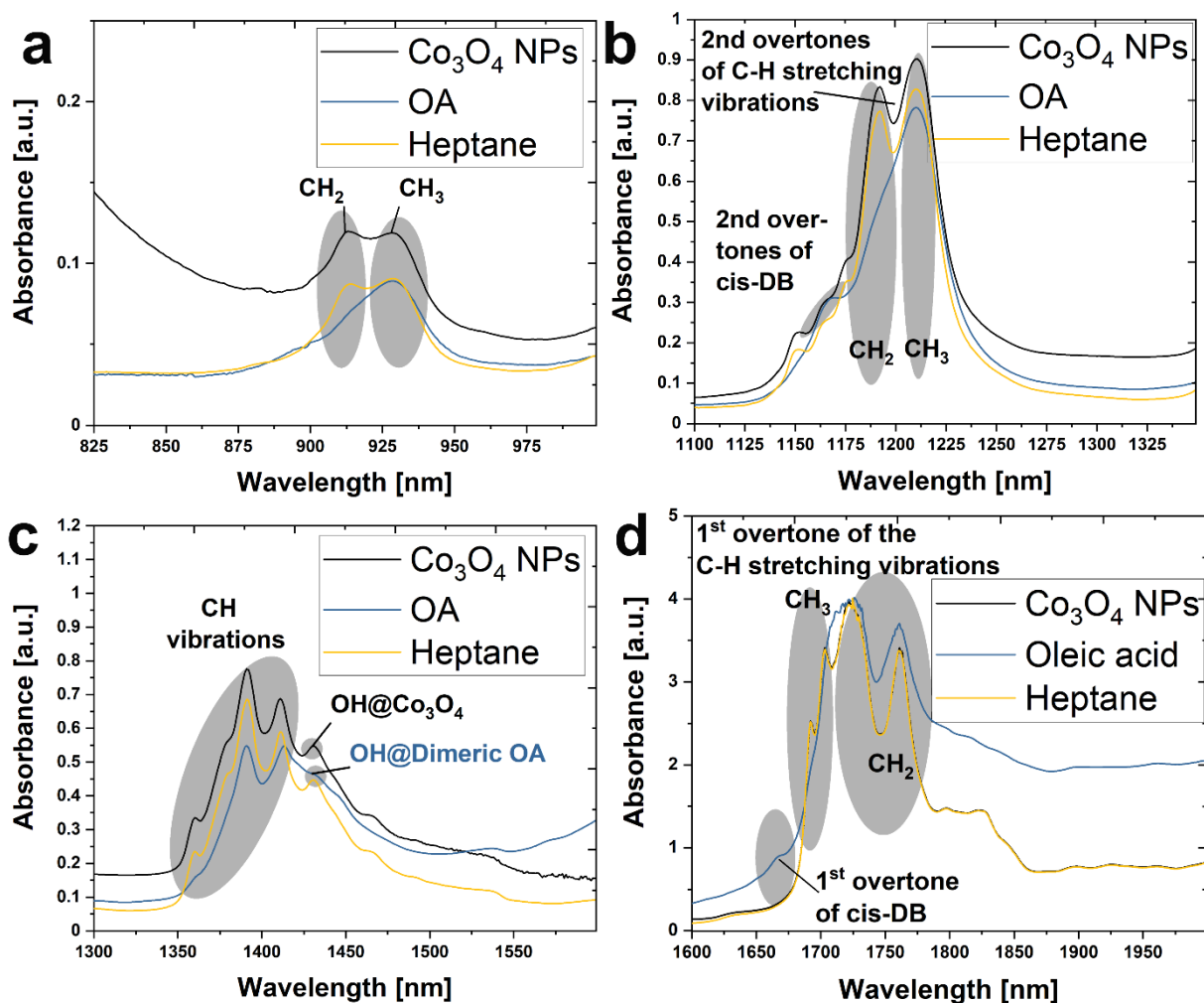
Figure S12: Enlarged views of specific regions in the UV-vis and NIR absorption spectra of a Co_3O_4 NP dispersion in heptane. The spectra of heptane and oleic acid (OA) are shown for comparison. a) Third overtones of the methyl and methylene stretching vibrations. b) Second overtones of the methyl and methylene stretching vibrations as well as the second overtone of the cis-double bond vibration of OA. c) C-H bond vibrations and O-H stretching vibration in pure OA and surface-bound OA. d) First overtones of the methyl and methylene stretching vibrations as well as the first overtone of the cis-double bond in OA.

Literature sources addressing the NIR absorption of heptane and oleic acid commonly represent the spectra as plots of absorbance *vs.* wavenumber (instead of absorbance *vs.* wavelength). A spectrum complementary to Figure 4 in the main text with the abscissa rescaled to wavenumbers is shown in **Figure S13** for better comparability.
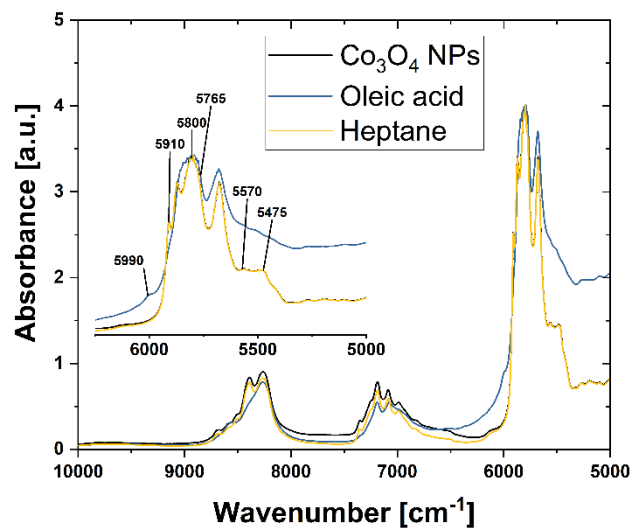
Figure S13: NIR spectra of Cb13 Co_3O_4 NPs as well as pure oleic acid and heptane. The NIR absorbance was plotted against wavenumbers to allow for easier comparison to existing literature.

2.12 Size-dependent absorption characteristics

In view of technological applications, size-dependent functional properties play a critical role in nanoscale materials. In this respect, the analysis of bandgap absorbance (at the peak maximum) provides a readily accessible insight into the presence and extent of size-related modulations of the electronic properties in nanomaterials.[19] Peak maxima of absorption bands assigned to the O^{2-} (2p)→$Co^{3+}(e_g)$ and O^{2-}(2p)→$Co^{3+}(t_{2g})$ transitions are summarized in **Table 2** for NPs with diameters between 2.8-10.9 nm revealing a size-dependent blue-shift with decreasing particle diameter. Specifically, the signal centered at 390 nm in 10.9 nm NPs exhibits a mild shift towards a lower wavelength of 369 nm when the particle size is reduced to 2.8 nm. A similar tendency is observed for the band detected at 677 nm.

Comparison with literature data obtained from larger NPs and thin films supports the observed trend (**Tab. 2**). Makhlouf *et al.* synthesized Co_3O_4 NPs in the size range of 15-55 nm with a broad size distribution by calcination of a Co-hydroxide precursor at different temperatures.[20] For particles with 15.8 nm and 31.3 nm diameters, the band maxima of the O^{2-}(2p)→$Co^{3+}(e_g)$ and O^{2-}(2p)→$Co^{3+}(t_{2g})$ transitions are located at ~425 nm/~725 nm and ~500 nm/~775 nm, respectively (position estimated based on the published spectrum).[20] Complementary data obtained from thin films with a thickness of 22 nm were reported as 441 nm/756 nm by Jiang *et al.*.[21] Please note, that while the general comparability between the here-reported absorption data and the literature values is reliable in the sense that a systematic trend is observed, the absolute values of peak positions may be affected by the presence of OA ligands as well as the highly diluted regime of our isolated NPs potentially decreasing the long-range exchange interactions between the individual grains in comparison to solid specimens.

Generally, the strong absorption by charge transfer across the entire visible spectral range renders Co_3O_4 NPs above a size of 7.2 nm an excellent photo-absorber material, thus facilitating applications in photocatalysis where Co_3O_4 acts as a co-catalyst in solar-driven water splitting. Furthermore, the existence of a systematic blue-shift of the Co_3O_4 O^{2-}(2p)→$Co^{3+}(e_g)$ and O^{2-}(2p)→$Co^{3+}(t_{2g})$ transitions demonstrates that the particles possess size-dependent absorption properties at the ~3-30 nm length scale.

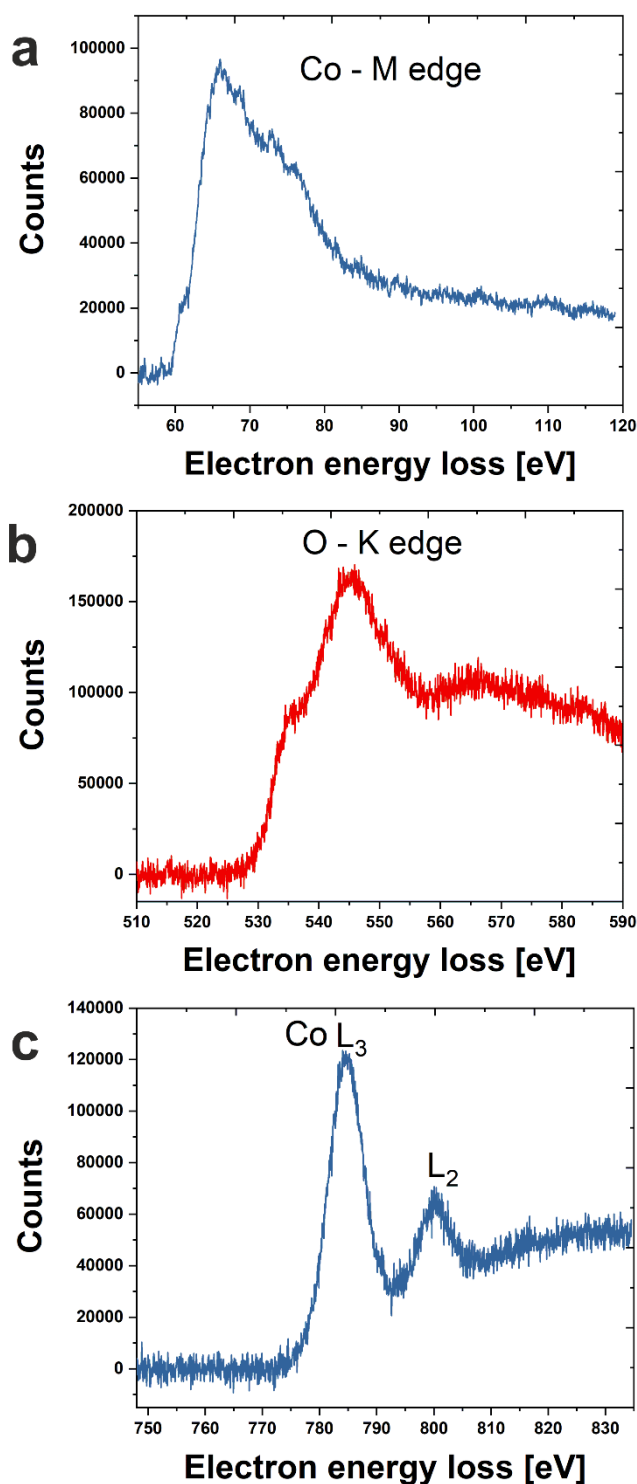## 2.13 Electron energy loss spectroscopy of Co_3O_4 nanoparticles

Figure S14: EELS spectra for the investigation of the molecular structure of Co_3O_4 nanoparticles. a) Co-M edge, b) O-K edge, c) Co-L_2 and -L_3 edges.

Electron energy-loss spectra (EELS) were recorded for Cb13 NPs immobilized on a carbon-coated copper TEM grid (**Figure S14**). Distinct signals characteristic of the electronic structure of Co_3O_4 are observed at 60 eV (cobalt M-edge, **Figure S14a**) and 540 eV (oxygen K-edge, **Figure S14b**) as well as 784 eV and 800 eV (cobalt L_3- and L_2-edges, **Figure S14c**).[22,23] No contributions of Fe or Ni impurities were observed around the L edges of Co. The oxygen K-edge exhibits a distinct profile shape indicative of Co_3O_4 (**Figure S14b**). Zhang *et al.* have demonstrated that thin Co_3O_4 layers are oxygen-depleted near the edge while thin CoO is oxygen-rich.[23] For this reason, a strong white line expected for the O-K edge of Co_3O_4 around 530 eV is not observed. The resulting peak shape is similar to the signal of the here investigated NPs depicted in **Figure S14**. Further information about the electronic composition of the sample may also be obtained from the L_3 and L_2 white lines. The spacing between both peaks amounts to 15.4 eV for the presented sample. The expected value for Co_3O_4 was reported as 15.5 eV and is in good agreement with the experiment. The peak separation expected for CoO, in contrast, is 16 eV, thus indicating the presence of phase-pure Co_3O_4.[22,24] The L_3/L_2 intensity ratio may provide additional information about the oxidation state of the material. The bulk values of Co_3O_4 and CoO are reported as 2.42 and 4.51, respectively,[24] where this significant difference is explained by different populations and spin-orbit couplings of the $2p_{1/2}$ and $2p_{3/2}$ states for varying amounts of Co(II) and Co(III) ions. After baseline correction according to the

Tougaards method, effective peak heights were extracted for the sample depicted in **Figure S14c,** and the L_3/L_2 intensity ratio was determined as 2.71.[25] While according to Zhao *et al.*, the L_3/L_2 ratio cannot easily differentiate between CoO and Co_3O_4 when observing very thin layers (analogous to very small particles), but the L_3/L_2 ratio of 2.71 indicates a slight increase of Co(II) ions compared to the stoichiometric spinel structure of Co_3O_4. In summary, the spectrum conforms well with the expected results for Co_3O_4. Hence, the EELS results support the assessment that Co_3O_4 has indeed been successfully synthesized.

2.14 Oleic acid-free nanoparticles prepared for electrocatalytic water splitting

Oleic acid-free nanoparticles were used to determine the potential of Co_3O_4 NPs in the electrocatalytic splitting of water (**Fig. 6**). The average particle size was determined by TEM as 11.28 ± 2.33 nm.
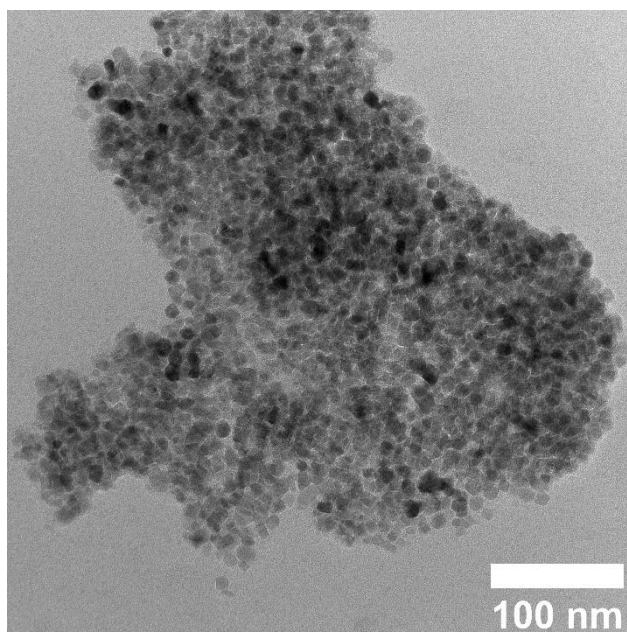

Figure S15: TEM micrograph of oleic acid-free nanoparticles prepared for electro-catalytic water splitting.

2.15 Structural analysis of a commercial Co_3O_4 nanopowder investigated for reference by cyclic voltammetry

Figure S16 displays transmission electron micrographs of a commercial Co_3O_4 nanopowder with a nominal particle size of < 50 nm obtained from Sigma Aldrich and used as reference material in water oxidation catalysis. An overview image reveals overall particle dimensions between ~16 nm and ~105 nm (**Figure S16a**).

The sample appears to comprise smaller primary grains in the size range between 10 nm and 40 nm fused into larger aggregates with irregular shapes *via* concave connections (**Figure S16b**). High-resolution TEM reveals a continuous crystal lattice within the larger particles as represented by lattice fringes with a characteristic inter-plane distance of 2.3 Å (determined by fast Fourier transformation) attributable to the {222} plane of the Co_3O_4 unit cell (**Figure S16c**).
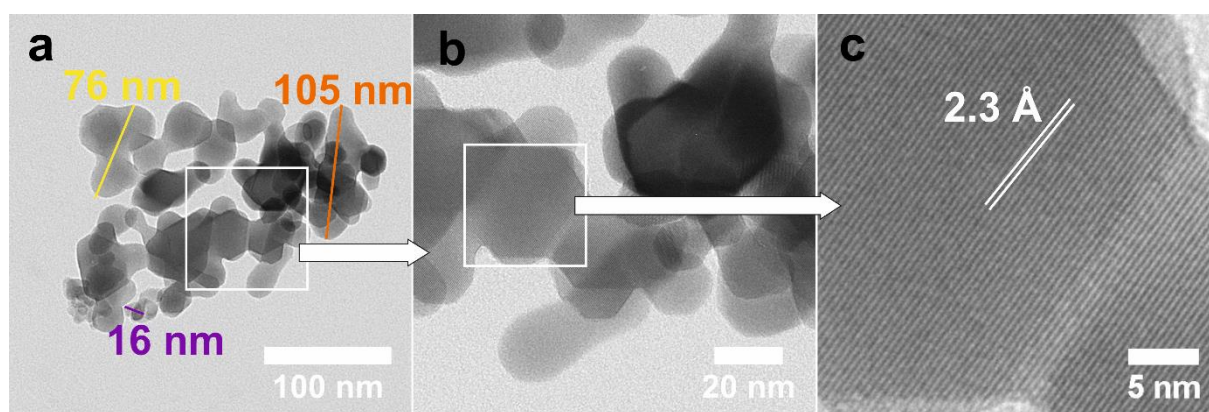

Figure S16: TEM micrographs of a commercial spinel cobalt oxide nanopowder obtained from Sigma Aldrich. a) Representative overview image revealing overall particle sizes ranging from 16-105 nm. b) Enlarged view of the area marked by a white box in a) showing grain boundaries between primary particles of 10-40 nm size. c) Enlarged view of the selected region in b) by high-resolution TEM showing lattice fringes. The characteristic distances between these uni-directional lattice fringes are attributed to the {222} plane of spinel cobalt oxide.

2.16 Reproducibility of the NP-catalyzed oxygen evolution reaction

In order to evaluate the reproducibility of the overpotential as a figure of merit for the electrocatalytic performance of the produced nanoparticles, all electrochemical measurements were replicated multiple times. Most importantly, to test the consistency of the electrode preparation protocol, several working electrodes were fabricated from the same batch of a Co_3O_4 nanopowder of cuboidal particles (Cb13-2). The results of four exemplary measurements obtained with independently prepared glassy carbon working electrodes are plotted in **Figure S17**.

Overpotentials (η) towards the oxygen evolution reaction (OER) were determined from the voltammograms at a current density of $J = 10$ mA/cm^2. The obtained values for Cb13-2 particles spanned a range from η = 410 mV (lowest) to η = 453 mV (highest), which demonstrates the very good reproducibility of the electrochemical measurements with only a small deviation around the average of η = 431.5 ± 17.6 mV (compare **Figure 6**, main text).
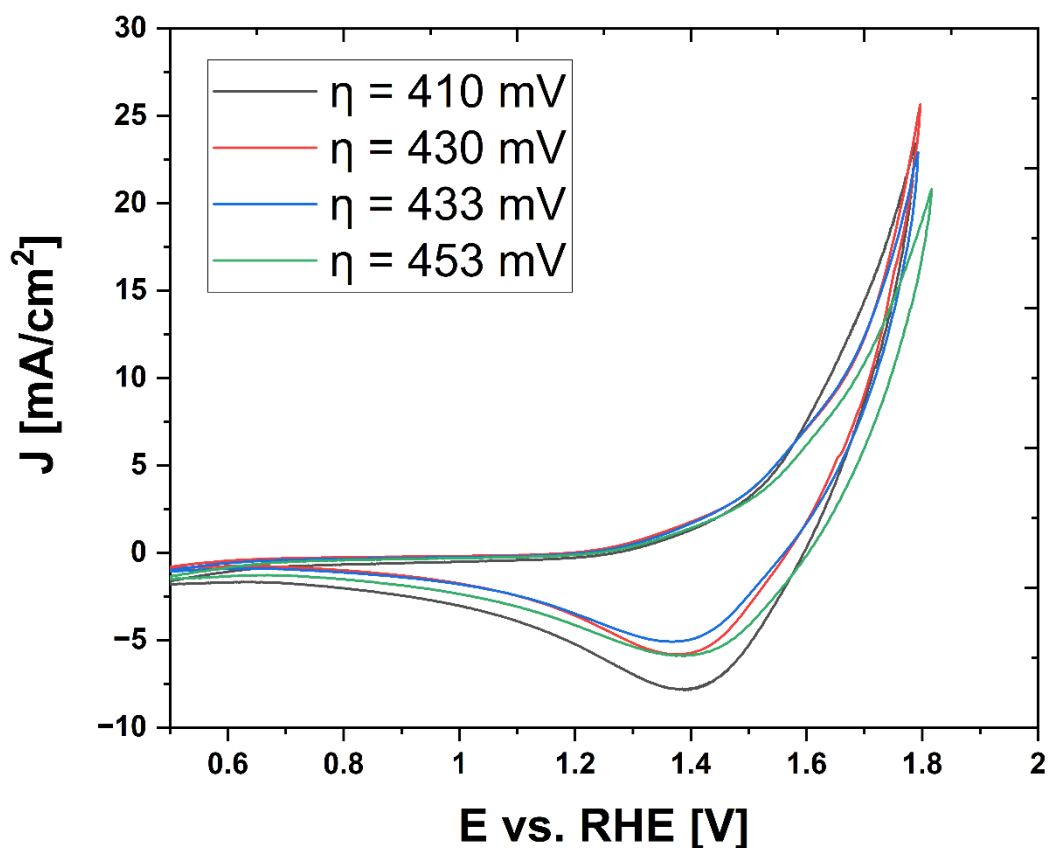

Figure S17: Exemplary cyclic voltammograms obtained from four independently prepared glassy carbon rotating disc electrodes coated with Cb13-2 NPs are shown to demonstrate the reproducibility of the electrochemical measurements performed for the determination of the average overpotential (η) of the NPs towards the electrocatalytic oxygen evolution reaction.

3. References

1 Z. P. Xu and H. C. Zeng, *Chem. Mater.*, 1999, **11**, 67–74.

2 Z. Liu, R. Ma, M. Osada, K. Takada and T. Sasaki, *J. Am. Chem. Soc.*, 2005, **127**, 13869–13874.

3 A. Pérez, J.-F. Lamonier, J.-M. Giraudon, R. Molina and S. Moreno, *Catal. Today*, 2011, **176**, 286–291.

4 R. Ma, Z. Liu, K. Takada, K. Fukuda, Y. Ebina, Y. Bando and T. Sasaki, *Inorg. Chem.*, 2006, **45**, 3964–3969.

5 K. Xiao, L. Zhang, Q. Tang, B. Fan, A. Hu, S. Zhang, W. Deng and X. Chen, *J. Solid State Electrochem.*, 2018, **22**, 2321–2328.

6 S. Kittaka, N. Uchida, I. Miyashita and T. Wakayama, *Colloids and Surfaces*, 1989, **37**, 39–54.

7 R. G. Delaplane, J. A. Ibers, J. R. Ferraro and J. J. Rush, *J. Chem. Phys.*, 1969, **50**, 1920–1927.

8 Y. Du, K. M. Ok and D. O'Hare, *J. Mater. Chem.*, 2008, **18**, 4450.

9 H. T. Phan and A. J. Haes, *J. Phys. Chem. C*, 2019, **123**, 16495–16507.

10 M. Barani, R. Bonetti and W. O. Parker, *J. Am. Oil Chem. Soc.*, 2023, 1–10.

11 S. A. Tovstun and V. F. Razumov, *J. Nanoparticle Res.*, 2017, **19**, 8.

12 D. Li, H. Yun, B. T. Diroll, V. V. T. Doan-Nguyen, J. M. Kikkawa and C. B. Murray, *Chem. Mater.*, 2016, **28**, 480–489.

13 D. R. Lide and G. Baysinger, *CRC Handbook of Chemistry and Physics*, CRC Press, 90th edn., 2010.

14 U. Liddel and C. Kasper, *Bur. Stand. J. Res.*, 1933, **11**, 599–618.

15 M. Buback and A. A. Harfoush, *Zeitschrift für Naturforsch. A*, 1983, **38**, 528–532.

16 L. Liu, Y. Cheng, X. Sun and F. Pi, *Spectrochim. Acta Part A Mol. Biomol. Spectrosc.*, 2018, **197**, 153–158.

17 M. Iwahashi, M. Suzuki, M. A. Czarnecki, Y. Liu and Y. Ozaki, *J. Chem. Soc. Faraday Trans.*, 1995, **91**, 697.

18 K. Koashi, M. Iwahashi and Y. Ozaki, *Appl. Spectrosc.*, 2003, **57**, 1539–1550.

19 S. Baskoutas and A. F. Terzis, *J. Appl. Phys.*, 2006, **99**, 013708.

20 S. A. Makhlouf, Z. H. Bakr, K. I. Aly and M. S. Moustafa, *Superlattices Microstruct.*, 2013, **64**, 107–117.

21 C.-M. Jiang, L. R. Baker, J. M. Lucas, J. Vura-Weis, A. P. Alivisatos and S. R. Leone, *J. Phys. Chem. C*, 2014, **118**, 22774–22784.

22 D. Barreca, A. Gasparotto, O. I. Lebedev, C. Maccato, A. Pozza, E. Tondello, S. Turner and G. Van Tendeloo, *CrystEngComm*, 2010, **12**, 2185.

23 Z. Zhang, *Ultramicroscopy*, 2007, **107**, 598–603.

24 Y. Zhao, T. E. Feltes, J. R. Regalbuto, R. J. Meyer and R. F. Klie, *J. Appl. Phys.*, 2010, **108**, 063704.

25 S. Tougaard, *Surf. Sci.*, 1989, **216**, 343–360.